JACS
JOURNAL OF THE AMERICAN CHEMICAL SOCIETY
pubs.acs.org/JACS
Article

^{99}Ru Solid-State Nuclear Magnetic Resonance Spectroscopy of Organometallic Compounds: Linking Nuclear Magnetic Resonance Parameters with Metal−Ligand Bonding

Sean T. Holmes, Yijue Xu, Adam B. Philips, Sara Termos, James J. Kimball, Jochen Autschbach,* and Robert W. Schurko*

Cite This: J. Am. Chem. Soc. 2025, 147, 20865−20877
Read Online
ACCESS | Metrics & More | Article Recommendations | Supporting Information

ABSTRACT: This study introduces ^{99}Ru solid-state NMR (SSNMR) spectroscopy, along with relativistic density functional theory (DFT) calculations of ^{99}Ru chemical shift and electric field gradient (EFG) tensors and their analysis with localized molecular orbitals, as a versatile tool to elucidate relationships between SSNMR spectra and Ru-ligand bonding in organometallic compounds. ^{99}Ru is a very challenging target for analysis by SSNMR. Robust experimental protocols were developed for the acquisition of ultrawideline ^{99}Ru SSNMR spectra for stationary samples with unprecedented signal-to-noise ratios and uniformity. The ^{99}Ru EFG and chemical shift tensors determined from these spectra are complemented by DFT-based analyses of the contributions of individual bond-, lone-pair-, and core-shell-orbitals to the NMR interaction tensors, which highlight their relationships with Ru-ligand bonding and electronic structure. These experimental and computational protocols are anticipated to prove fruitful for the characterization of a wide range of Ru-containing compounds, with applications to catalysis, advanced materials, and electronic devices.

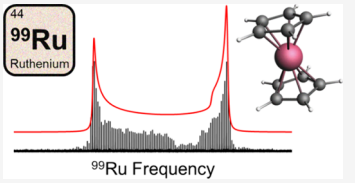

1. INTRODUCTION

Ruthenium (Ru), a member of the platinum group elements (PGEs), is critical for the production of electronic devices and molecular sensors, and also has many applications in chemical catalysis.[1−4] Like all PGEs, Ru is a rare (*ca.* 1 ppb in the Earth's crust) and costly metal that faces issues of limited supply chains, geopolitical distribution, and environmental challenges associated with its extraction and recycling. However, due to the unique properties of PGEs in coordination chemistry and numerous concomitant critical applications,[5,6] it is of great importance to elucidate the electronic structures of PGE coordination compounds, including the nature of PGE-ligand bonds, to better understand their emergent functionality, and to potentially identify suitable replacement metals that are less costly and more readily available.[7]

Because of their unique electronic valence structures, we hypothesize that PGEs such as Ru differ from other transition metal elements in how they engage coordinating ligand atoms in *covalent bonding*, i.e., via *dative* or *donation* bonding, including both ligand-to-metal donation and metal-to-ligand back-donation.[8,9] Donation bonding influences the structure and reactivity of PGE coordination compounds, with the degrees of covalent and ionic bonding character impacting emergent physicochemical properties and functionality within catalysts and advanced materials. In Ru coordination compounds, the nature of these bonds may be the primary driver behind their unique properties, complementing other factors such as atomic radii, electrochemical properties, preferred oxidation states, and coordination environments. A proof of concept is furnished by our recent study of coordination compounds with another PGE, *viz.* rhodium, by ^{103}Rh solid-state NMR (SSNMR) spectroscopy and quantum chemical computation.[10] We propose that the combination of ^{99}Ru SSNMR and density functional theory (DFT) calculations with a relativistic Hamiltonian provides a similarly powerful avenue for interpreting electronic structure and bonding in Ru coordination compounds, hypothetically enabling significant advances in the study of PGEs and the search for replacement metals. However, SSNMR experiments prove to be far more challenging with ^{99}Ru than with ^{103}Rh.

^{99}Ru is among the most unreceptive NMR nuclides in the Periodic Table, with a spin of $I = 5/2$, a low gyromagnetic ratio of $\gamma = -1.229 \times 10^7$ rad T^{-1} s^{-1}, a moderate quadrupole moment of $Q = 7.9$ fm^2, and a low natural abundance of 12.76%.[11] Literature reporting ^{99}Ru SSNMR spectroscopy as a characterization technique is scarce, with most publications related to metals and intermetallic materials.[12−18] To our knowledge, there is only one study describing the use of ^{99}Ru SSNMR spectroscopy to characterize coordination compounds. In this seminal study, Ooms and Wasylishen[19] reported ^{99}Ru SSNMR spectra of the inorganic compounds $K_4[Ru(CN)_6]\cdot xH_2O$ ($x = 0$, 3) and $Ru_3(CO)_{12}$. In these

Received: March 19, 2025
Revised: May 7, 2025
Accepted: May 8, 2025
Published: June 5, 2025

materials, Ru atoms are in sites of octahedral or pseudo-octahedral symmetry, which results in small quadrupolar coupling constants and minimal chemical shift anisotropies that manifest in the SSNMR spectra as relatively narrow powder patterns. However, to make the acquisition of ^{99}Ru SSNMR spectra tenable for a wider range of materials with different Ru coordination environments, including organometallic compounds used in catalysis or as catalytic precursors, significant improvements in techniques for acquiring high-quality ^{99}Ru SSNMR spectra are necessary.

The acquisition of ^{99}Ru SSNMR spectra of organometallic complexes is challenging because of heterogeneous broadening of central transition (CT, $+1/2 \leftrightarrow -1/2$) powder patterns due to the chemical shift anisotropy and second-order quadrupolar interactions (SOQI), which can result in patterns with breadths of hundreds of kHz or greater and inherently impact signal-to-noise (S/N). To address some of the challenges associated with the acquisition of wide-line and ultrawideline SSNMR powder patterns, frequency-swept wideband, uniform rate, smooth truncation (WURST) pulses[20] are now widely used for broadband excitation, refocusing, and polarization transfer.[21−23] When samples feature favorable transverse relaxation characteristics (i.e., effective T_2 values, T_2^{eff}, are long enough to exploit the detection of refocused spin polarization using a CPMG-type experiment), WURST pulses can be incorporated into Carr−Purcell−Meiboom−Gill (CPMG)-type pulse sequences[24−26] for the purpose of T_2-based signal enhancement, forming the basis of the WURST-QCPMG pulse sequence and its variants.[27,28] Furthermore, the broadband adiabatic inversion cross-polarization (BRAIN-CP) pulse sequence can be used to increase signal via polarization transfer from protons,[29−32] with a theoretical maximum signal gain proportional to $\gamma(^1\text{H})/\gamma(^{99}\text{Ru}) \approx 21.7$. Nonetheless, there are difficulties associated with the efficient transfer of spin polarization to half-integer quadrupolar nuclides (HIQNs) such as ^{99}Ru,[33−35] some of which are discussed in this work. Finally, the increasingly available modern "GHz class magnets" (e.g., the one-of-its-kind 36 T Series Connected Hybrid [36T-SCH] magnet at the National High Magnetic Field Laboratory [NHMFL] and new commercial GHz-class NMR platforms around the world)[36,37] may prove critical for the acquisition, analysis, and interpretation of ^{99}Ru SSNMR spectra, because CT powder patterns undergo narrowing proportional to B_0^{-1} (albeit with the caveat that chemical shift anisotropy increases pattern breadths proportional to B_0, though this is not anticipated to be an issue for ^{99}Ru, where in most cases, the effect of the second-order quadrupolar interaction far outweighs that of CSA). Hence, this combination of pulse sequences and hardware has the potential to yield ^{99}Ru SSNMR spectra with powder patterns of unprecedented intensity and uniformity.

Quantum chemical calculations are crucial for relating SSNMR data with electronic structure, chemical bonding, and emergent functionality.[10,38−41] Given the sensitivity of NMR interaction tensor calculations to the approximations that are inevitably necessary in the description of the electronic structure, DFT with hybrid functionals has long been the method of choice. Furthermore, for calculations involving heavy metal elements, including all of the PGEs, it is necessary to perform the calculations with a relativistic Hamiltonian.[10,42,43] Although there are several reports of DFT calculations of ^{99}Ru chemical shifts, electric field gradients (EFGs), and/or spin−spin coupling constants for isolated molecules or molecules in solution,[44−49] only the study by Ooms and Wasylishen provides calculations of these parameters for solids.[19] Fortunately, recent advances have been made in the computation of NMR tensor parameters for heavy fourth- and fifth-period elements, especially with regard to protocols employing the zeroth-order regular approximation (ZORA) Hamiltonian and hybrid DFT.[50−56] We anticipate that such methods will prove fruitful for the accurate prediction of ^{99}Ru chemical shift and EFG tensors in a wide array of materials.

Computational analyses based on localized molecular orbitals are being increasingly used to investigate the origins of NMR interactions tensors in terms of electronic structure, including the contributions from individual bonding/antibonding, lone-pair, and core orbitals.[57−60] Such orbital-based analyses allow, for instance, to quantify the effects from ligand-to-metal donation and metal-to-ligand back-donation via more or less pronounced delocalization of ligand/metal lone pairs onto the metal/ligand, which provides an intuitive picture of the effects of bonding on the NMR tensors at the metal sites.

In this study, we provide the first examples of ultrawideline ^{99}Ru SSNMR spectra of Ru coordination compounds. These experiments take advantage of 18.8 T and 36T-SCH magnets at the NHMFL, as well as SSNMR probes adapted in-house for low-γ experimentation. The ^{99}Ru chemical shift and EFG tensors obtained from these measurements are compared to those obtained from calculations using state-of-the-art relativistic DFT-based calculations. Analyses of these tensors in terms of localized orbitals permits exploration of their relationships to electronic structure and bonding. It is anticipated that these methods will lend deeper insight into the unique physicochemical properties of PGE coordination compounds, and open avenues for routine experimental and theoretical applications of ^{99}Ru SSNMR spectroscopy.

2. EXPERIMENTAL AND COMPUTATIONAL DETAILS

2.1. Samples. Samples were used as-received from Strem Chemicals, Inc. Their identities and purities were confirmed through comparison of experimental and simulated PXRD patterns based on known crystal structures (see Figure S1 in the Supporting Information).[61−63]

2.2. Solid-State NMR Spectroscopy. *Overview.* SSNMR spectra were collected at the NHMFL in Tallahassee, FL. Spectra were obtained at 18.8 T using a Bruker Avance NEO console, and medium-bore Oxford magnets, with Larmor frequencies of $\nu_0(^1\text{H})$ = 799.7 MHz and $\nu_0(^{99}\text{Ru})$ = 36.7 MHz. Other experiments were conducted using the 36 T SCH[36] magnet (operating at 35.2 T for NMR) and a Bruker Avance NEO console, with Larmor frequencies of $\nu_0(^1\text{H})$ = 1.500 GHz and $\nu_0(^{99}\text{Ru})$ = 69.1 MHz. All spectra were acquired using NHMFL-built 5.0 mm HX probes with samples packed into airtight 5.0 mm o.d. ^{1}H-free sample containers. Acquisition parameters are summarized in the Supporting Information (Table S1 - S3). Pulse sequences and recommended calibration parameters and standards are available online at https://github.com/rschurko.

^{99}Ru WURST-QCPMG Experiments. The majority of ^{99}Ru spectra were acquired using the WURST-QCPMG pulse sequence.[27,28] Spectra were acquired at both B_0 = 18.8 and 35.2 T. The sweep widths of the excitation and refocusing pulses were set to *ca.* 1.5 to 2 times the target pattern breadth. Recycle delays were chosen that maximized the signal-to-noise ratio per unit time. In some cases, spectra were collected with ^{1}H continuous wave decoupling, depending on the trade-off between wear on the probe due to long acquisition times and maximizing the collection of refocused spin polarization (i.e., the number of Meiboom-Gill loops).

https://doi.org/10.1021/jacs.5c04759
J. Am. Chem. Soc. 2025, 147, 20865−20877

^{1}H−^{99}Ru BRAIN-CP Experiments. A spectrum of Cp_2Ru was acquired at 18.8 T using the BRAIN-CP pulse sequence.[29−31] Because of the slow rate of cross relaxation during CP owing to the relatively low values of $\gamma(^{99}Ru)$ and the heteronuclear dipolar coupling constant, $R_{DD}(^{99}Ru, ^1H)$,[64,65] a contact time of 30 ms was used.[66] The sweep widths of the contact, excitation, and refocusing pulses were set to 400 kHz. The maximum amplitude of the ^{1}H spin-lock pulse was set to $\nu_2(^1H)$ = 30 kHz. An optimized ^{1}H recycle delay of 1.0 s was used. A 16-step phase cycling scheme that allows for coherent CP transfer was used.[67] Spectra were acquired with ^{1}H continuous wave decoupling with rf amplitudes of 25 kHz. A flip-back pulse,[68,69] which involves the application of an additional $\pi/2$ pulse on the ^{1}H channel following ^{99}Ru acquisition to return the ^{1}H transverse magnetization to its equilibrium orientation, was used to reduce recycle delays.

Spectral Processing and Fitting. ^{99}Ru chemical shifts were referenced to 0.3 M $K_4Ru(CN)_6$ in D_2O at $\delta_{iso}(^{99}Ru)$ = 0 ppm using solid $[Ru(NH_3)_6]Cl_2$ at $\delta_{iso}(^{99}Ru)$ = 7569 ppm as a secondary reference (Figure S2).[19] Spectra were processed with a Fourier transformation followed by a magnitude calculation in the Bruker TopSpin v4.1.4 program. Numerical simulations were conducted with the ssNake software package[70] and verified through additional simulations using WSolids1.[71] Uncertainties in the quadrupolar and chemical shift tensor parameters were assessed via bidirectional variation of each parameter, and visual comparison of experimental and simulated spectra.

2.3. Computational Details. *Geometry Optimizations.* Refinements of structural models initially determined through X-ray diffraction were performed using plane-wave DFT as implemented in the CASTEP module of BIOVIA Materials Studio 2020.[72] The positions of all atoms were relaxed using the LBFGS energy-minimization scheme,[73] in which lattice parameters remained fixed at the given experimental values from X-ray diffraction data.[61−63] Calculations used the Perdew−Burke−Ernzerhof (PBE) functional,[74] a plane wave cutoff energy of 800 eV, a *k*-point spacing of 0.05 Å^{-1},[75] ZORA ultrasoft pseudopotentials generated on the fly,[76] and an SCF convergence threshold of 5×10^{-7} eV. Dispersion was included through the many-body dispersion force field of Tkatchenko et al.[77] Thresholds for structural convergence include maximum changes of: 5×10^{-6} eV atom^{-1} for energy; 5×10^{-4} Å atom^{-1} for displacement; and 10^{-2} eV Å^{-1} for Cartesian forces.

EFG and Magnetic Shielding Tensors. ^{99}Ru EFG and magnetic shielding tensors were calculated using Amsterdam Density Functional (ADF) program within the Amsterdam Modeling Suite (AMS 2021.106).[78,79] The EFG calculations and analyses included relativistic picture change corrections ('ZORA-4') as devised by van Lenthe et al.[80] Calculations of magnetic shielding tensors employed the gauge-including atomic orbital (GIAO) method,[81,82] as implemented in AMS.[83−87] Calculations used either the PBE[74] or hybrid PBE0[88] functional, and the ZORA Hamiltonian in its scalar relativistic (SR) variant or including both SR effects and the spin−orbit (SO) interaction.[89−93] The NMR calculations included the perturbation of the pure-DFT exchange-correlation potential response kernel (fXC keyword).[94] Calculations using hybrid variants of PBE (PBE0)[95] also explored the effects of differing admixtures of exact exchange (eX) (i.e., 25% and 12.5%). Calculations used isolated molecules, with geometries refined using plane-wave DFT, as structural models. A multiple-layer ('locally dense') Slater-type orbital (STO) basis set partitioning scheme was used: for the Ru atom and all atoms bonded to it, the TZ2P basis set was used,[96] along with Becke integration set to "good";[97,98] all remaining non-hydrogen atoms and hydrogen atoms were assigned the basis sets DZP and DZ, respectively, with Becke integration set to "normal".

NLMO Analysis. Hybrid-functional Kohn−Sham (KS) DFT calculations of the ^{99}Ru EFG and magnetic shielding tensors were performed with the ADF program included in AMS version 2024.101. Structures for the complexes were taken from the experimental crystal structures followed by an all-atom optimization with CASTEP. These calculations were performed using the PBE0 functional with the admixtures of eX set to 12.5%. For each complex, an initial single-point calculation was performed to obtain the canonical MOs. Scalar relativistic natural localized MOs (NLMOs) were generated subsequently with the NBO algorithmic framework[99] as implemented in the NBO 7.0 program.[100] This step was followed by another SR-ZORA ADF single-point calculation with accompanying analysis of the EFG tensors at the Ru sites.[49] A separate single-point run including relativistic SO effects was also performed, along with the calculation of the nuclear shielding tensor and subsequent analysis in terms of the SR occupied and unoccupied NLMOs.[58,60] Energies for the NLMOs were obtained as the diagonal elements of the SR KS Fock matrix expressed in the basis of NLMOs. NLMO visualizations are in the form of isosurfaces at ±0.03 atomic units.

3. RESULTS AND DISCUSSION

3.1. ^{99}Ru SSNMR Spectroscopy. Three organometallic ruthenium coordination compounds were chosen for investigation based on the following criteria: (i) they are diamagnetic Ru^{II} compounds; (ii) they have a Ru wt% above 25% to maximize the number of ^{99}Ru spins; (iii) the compounds represent a variety of important structural motifs in ruthenium coordination chemistry, featuring terminal chlorine ligands and an assortment of π-coordinating ligands; and (iv) ^{1}H spins are present to explore the use of ^{1}H−^{99}Ru polarization transfer methods. These compounds are Cp_2Ru, Cp^*_2Ru, and Cp*ClRu(cod) [Cp = $C_5H_5^-$; Cp* = $C_5Me_5^-$; cod = 1,5-cyclooctadiene] (Scheme 1). For the acquisition of the WURST-QCPMG spectra, $[Ru(NH_3)_6]Cl_2$ serves as a standard for calibration of ^{99}Ru rf amplitudes due to the narrow powder pattern resulting from the octahedral symmetry of the Ru atom, as well as the short values of $T_1(^{99}Ru)$, which enables short recycle delays of 2.0 s. Similarly, the "horns" in the pattern of Cp_2Ru (*vide infra*) serve as a standard for the optimization of the Hartmann−Hahn matching conditions in the BRAIN-CP experiments, which are critical for obtaining undistorted ultrawideline powder patterns.

Scheme 1. Molecular Structures of Cp_2Ru, Cp^*_2Ru, and Cp*ClRu(cod) [Cp = $C_5H_5^-$; Cp* = $C_5Me_5^-$; cod = 1,5-Cyclooctadiene]

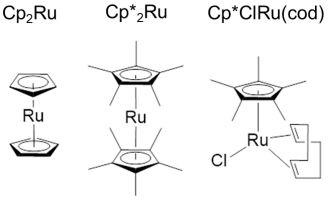

^{99}Ru SSNMR experiments were performed at fields of 18.8 and 35.2 T on static (i.e., nonspinning) samples. Relative to SSNMR experiments performed at 18.8 T, experimentation at 35.2 T using the SCH magnet provides signal enhancement due to the increased field strength, along with the added gain of narrowing the CT patterns (since the dominant broadening effects of the SOQI scale as B_0^{-1}). Furthermore, since the CT spectra of HIQNs such as ^{99}Ru can be influenced by both the SOQI and CSA, the acquisition of spectra at two fields allows for refinement of the ^{99}Ru EFG and chemical shift tensors, as well as the set of Euler angles defining the relative orientation of their principal axis systems.

The static ^{99}Ru spectra for the ruthenium coordination compounds are shown in Figures 1−3, whereas the EFG and chemical shift tensor parameters extracted from simulations of the spectra are given in Table 1. The spectra in Figures 1 and 2

https://doi.org/10.1021/jacs.5c04759
J. Am. Chem. Soc. 2025, 147, 20865−20877

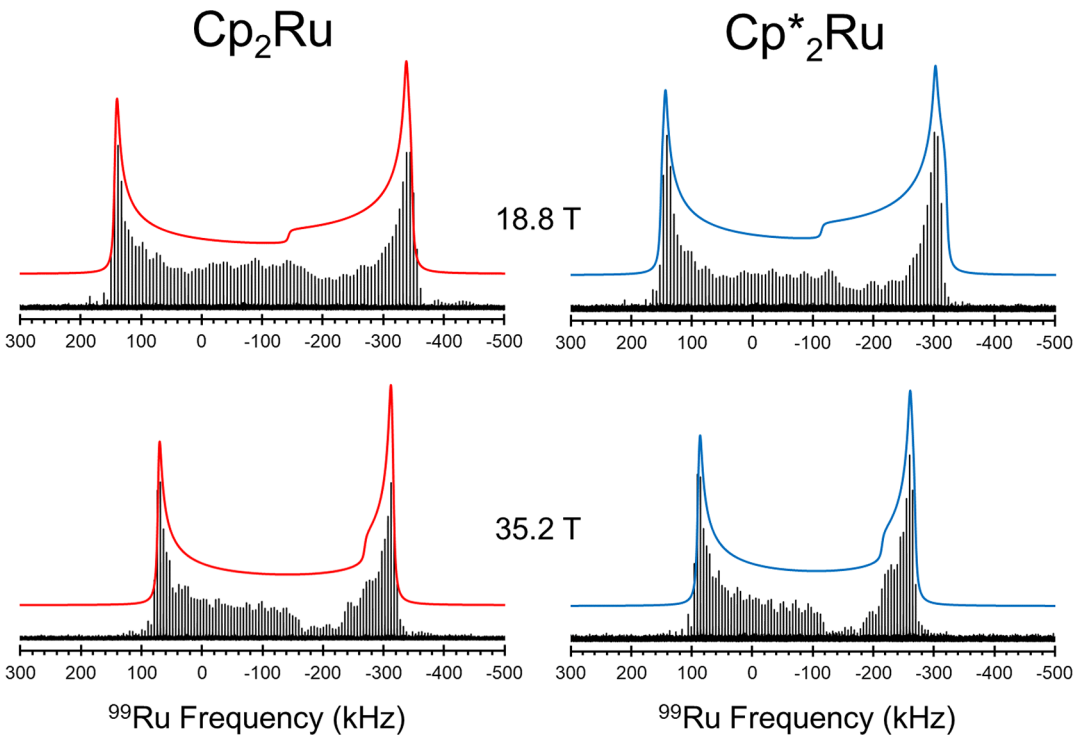

Figure 1. ^{99}Ru SSNMR spectra of Cp_2Ru and Cp^*_2Ru acquired using the WURST-QCPMG pulse sequence at B_0 = 18.8 and 35.2 T (black), along with the corresponding simulated patterns (red and blue).

Table 1. Experimental and Calculated ^{99}Ru EFG and Chemical Shift Tensors[a,b,c,d]

		C_Q (MHz)	η_Q	δ_{iso} (ppm)	Ω (ppm)	κ	α (°)	β (°)	γ (°)
Cp_2Ru	Exp	21.8(2)	0.02(2)	−1350(50)	3800(200)	1.0(1)	n/a[e]	0(5)	n/a[e]
	Calc	30.70	0.02	−1393	3717	0.99	180	0	90
Cp^*_2Ru	Exp	21.4(2)	0.04(2)	−900(50)	3300(200)	1.0(1)	n/a[e]	0(5)	n/a[e]
	Calc	31.85	0.01	−818	3521	0.99	202	0	272
Cp*RuCl(cod)	Exp	23.9(4)	0.76(4)	880(50)	2000(100)	0.5(3)	90(20)	90(5)	90(20)
	Calc	−29.88	0.75	842	2149	−0.21	59	85	108

[a]The experimental uncertainties in the last digit for each value are indicated in parentheses. [b]The principal components of the EFG tensors are defined such that $|V_{33}| \geq |V_{22}| \geq |V_{11}|$. The quadrupolar coupling constant and asymmetry parameter are given by $C_Q = eQV_{33}/h$, and $\eta_Q = (V_{11} - V_{22})/V_{33}$, respectively. The sign of C_Q cannot be determined from the experimental spectra. [c]The chemical shift tensors are defined using the frequency-ordered convention, in which the principal components are ordered $\delta_{11} \geq \delta_{22} \geq \delta_{33}$. The isotropic chemical shift, span, and skew parameter are given by $\delta_{iso} = (\delta_{11} + \delta_{22} + \delta_{33})$, $\Omega = \delta_{11} - \delta_{33}$, $\kappa = 3(\delta_{22} - \delta_{iso})/\Omega$, respectively. [d]The Euler angles α, β, and γ define the relative orientation of the EFG and chemical shift tensors using the $ZY'Z''$ convention for rotation. [e]This parameter has little-or-no discernible effect on the appearance of simulated powder patterns.

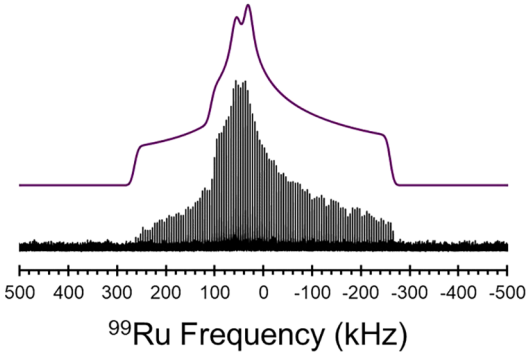

Figure 2. ^{99}Ru SSNMR spectrum of Cp*ClRu(cod) acquired using the WURST-QCPMG pulse sequence at B_0 = 35.2 T (black), along with the corresponding simulated pattern (purple).

were obtained using the WURST-QCPMG, whereas the spectrum in Figure 3 was obtained using the ^{1}H−^{99}Ru BRAIN-CP sequence. None of the spectra indicate the presence of impurity phases, and all feature patterns that are consistent with a single Ru site (in agreement with their crystal structures). In some of these spectra (i.e., those for Cp_2Ru and Cp^*_2Ru), there are small "dips" in the signal intensity that do not match the ideal simulations; these artifacts are common in the spectra of HIQNs acquired with frequency swept pulses,[32,101−104] resulting from population transfer from the ±3/2 and/or ±5/2 spin states for crystallites with particular EFG tensor orientations with respect to B_0.

The ^{99}Ru SSNMR spectra of Cp_2Ru and Cp^*_2Ru were acquired using the WURST-QCPMG pulse sequence (Figure 1). The spectra were collected using a single transmitter offset frequency, with total experiment times ranging between *ca.* 19 − 25 h at 18.8 T and 1.4 − 3.6 h at 35.2 T. Each powder

https://doi.org/10.1021/jacs.5c04759
J. Am. Chem. Soc. 2025, 147, 20865−20877

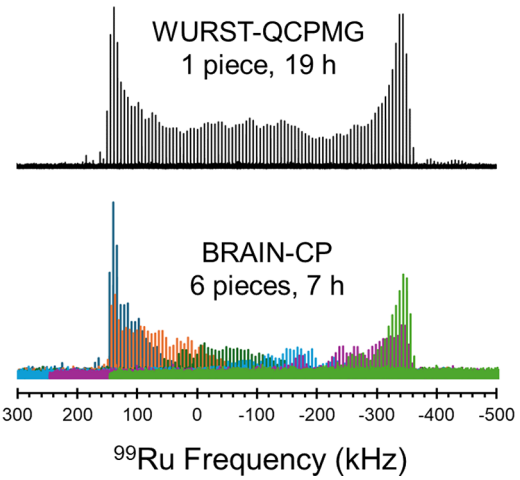

Figure 3. ^{99}Ru SSNMR spectra of Cp_2Ru acquired at B_0 = 18.8 T using the WURST-QCPMG (top) or BRAIN-CP (bottom) pulse sequences. The former spectrum was acquired in a single *ca.* 19 h experiment, whereas the latter spectrum was acquired using six separate experiments with varying transmitter offsets (each shown in a different color), leading to a total experiment time of *ca.* 7 h.

pattern is broad (*ca.* 500 kHz in breadth at 18.8 T, and *ca.* 400 kHz at 35.2 T) with influence from the SOQI and CSA interactions. Simulations of spectra acquired at two fields reveal that the C_Q values are similar (21.8 ± 0.2 and 21.4 ± 0.2 MHz for Cp_2Ru and Cp^*_2Ru, respectively) and the values of η_Q are both near zero (0.02 ± 0.02 and 0.04 ± 0.02, respectively), indicating EFG tensors of high axial symmetry and the orientation of V_{33} near the pseudo-C_5 rotational axes. However, the two materials have substantial differences in the chemical shift tensors: for Cp_2Ru, δ_{iso} = −1350 ± 50 ppm and Ω = 3800 ± 200 ppm, whereas for Cp^*_2Ru, δ_{iso} = −900 ± 50 ppm and Ω = 3300 ± 200 ppm. Both chemical shift tensors feature near-axial symmetry, as indicated by a value of κ = 1.0, as well as Euler angles of $\beta = 0 \pm 5°$, implying that the unique principal component, δ_{33}, which indicates the direction of highest magnetic shielding, is also oriented along or near the C_5 rotational axes in each case.

The ^{99}Ru SSNMR spectrum of Cp*ClRu(cod) was also acquired at 35.2 T using the WURST-QCPMG pulse sequence (Figure 2). This pattern is significantly broader than those of Cp_2Ru and Cp^*_2Ru acquired at the same field, with a breadth of *ca.* 530 kHz. Remarkably, this pattern was acquired in 2.1 h at 35.2 T. Unfortunately, the acquisition of the corresponding spectrum at 18.8 T did not prove practical due to its anticipated breadth (*ca.* 900 kHz) — however, this did not hinder our ability to simulate the 35.2 T spectrum and extract the relevant tensor parameters. The spectrum reveals a much higher isotropic chemical shift than those of the first two compounds (δ_{iso} = 880 ± 50 ppm). The magnitude of C_Q = 23.9 ± 0.4 MHz is also slightly larger in comparison to the first two compounds, and the value of η_Q is predicted to be 0.76 ± 0.04, reflecting the absence of axial symmetry in this coordination complex. In addition, the span (Ω = 2000 ± 100 ppm) of the chemical shift tensor is smaller than those of the metallocene compounds, and the skew indicates a lack of axial symmetry in the chemical shift tensor ($\kappa = 0.5 \pm 0.3$).

Finally, we acquired the ^{99}Ru spectrum of Cp_2Ru using the BRAIN-CP sequence (Figure 3). To facilitate these experiments, a long contact time of 30 ms was used for optimum ^{1}H→^{99}Ru polarization transfer, which is often necessary for low-γ nuclides.[10,66,105] However, to reduce the duty cycle of the probe, there is always a compromise between the length of the contact pulse and the number of Meiboom-Gill loops within a CPMG-type sequence, which must be carefully considered when setting up such an experiment. Due to the bandwidth of the probe (which is limited by the *Q*-factor), and the limited bandwidth of long contact pulses, it was not possible to acquire the ^{99}Ru spectrum of Cp_2Ru in a single experiment. Instead, a series of six subspectra were acquired using evenly spaced transmitter offset frequencies. Together, these individual subspectra trace out the complete powder pattern, with identical discontinuities to the pattern observed by the direct excitation (i.e., WURST-QCPMG) method in a single experiment. Significantly, the complete BRAIN-CP spectrum was obtained in *ca.* 7 h, whereas the WURST-QCPMG spectrum was obtained in *ca.* 19 h. This result provides confidence that indirect excitation methods utilizing polarization transfer from abundant spins presents a feasible pathway for acquiring high quality SSNMR spectra for low-γ HIQNs such as ^{99}Ru.

3.2. Quantum Chemical Calculations of ^{99}Ru EFG and CS tensors. The accurate theoretical prediction of NMR tensors provides crucial links between observed NMR parameters, electronic structure, metal−ligand bonding, and the emergent physicochemical properties and functionality of PGE coordination compounds. However, analysis of physicochemical properties is predicated on accurate calculated electronic structures that best reproduce the observed NMR tensors. To obtain the best agreement between experiment and theory, we assessed three considerations for calculations of ^{99}Ru magnetic shielding and EFG tensors of the Ru coordination compounds. First, we considered the importance of structural refinements through comparison of calculations of XRD-derived structures, structures where only the positions of hydrogen atoms have been refined, and structures in which the positions of all atoms have been refined. Second, we performed a series of calculations using SR or SO ZORA. Third, we compared the nonhybrid functional PBE and the hybrid PBE0, including the effects of different admixtures of eX in the latter. A summary of these calculations is provided in Tables S4 and S5, with correlation plots showing their relationships to experimental data in Figures S3 and S4.

Calculations on this limited number of systems allow the following conclusions: (i) all-atoms geometry optimizations were performed for all systems because of disorder in the position of a carbon atom in the XRD-derived structure of Cp^*_2Ru;[62] (ii) the inclusion of SO effects has a large impact on calculated magnetic shielding tensors; (iii) the hybrid functional PBE0 provides more accurate magnetic shielding tensors that the PBE functional. The differences in the performance of these functionals likely relates at least in part to the electron delocalization error (DE),[106] a well-known phenomenon in Kohn−Sham DFT, the effects of which vary with the functional approximations used, as well as the system under consideration. The inclusion of an admixture of eX in hybrid functionals (e.g., 25% in the standard PBE0 approximation) often greatly alleviates the DE, although this can also lead to an overcorrection, as seen here. We find that calculations performed at the PBE0/SO level with 12.5% eX lead to the best agreement with experiment, and are consequently used for the NLMO analyses (*vide infra*). These results are largely consistent with our previous work on other PGEs.[10] However,

https://doi.org/10.1021/jacs.5c04759
J. Am. Chem. Soc. 2025, 147, 20865−20877

we emphasize that these conclusions are derived from calculations on three organometallic compounds; our ongoing work on a larger variety of systems may provide a more robust set of computational protocols to achieve the best agreement between calculation and experiment.

The agreement between experimental and calculated chemical shift tensors is generally very good. For Cp_2Ru and Cp^*_2Ru, experiment and calculation are nearly identical (to within uncertainty), whereas for Cp*ClRu(cod), the errors are somewhat higher. The RMS error for the principal components for the three compounds is *ca.* 220 ppm, which is comparable to our previous work on ^{103}Rh.[10]

Although there is good qualitative agreement between calculated (in a.u.) and experimental (in MHz) EFG tensors, all computational methods led to overestimation of the magnitude of C_Q. For Cp_2Ru, the calculated value of V_{33} presented here (i.e., 1.654 a.u.) is similar to those in previous reports.[47,49] However, V_{33} has been determined independently from Mössbauer quadrupole splitting data, revealing a value of 1.15 a.u. Assuming $\eta_Q = 0$, this leads to C_Q of 21.3 MHz, which is similar to the experimental value of 21.8 MHz determined in the present work. The reevaluation of the $^{99/101}$Ru quadrupole moment has been the subject of several recent studies, although these seem to indicate an uncertainty of *ca.* 5% at most.[107−109] The calculated values of the asymmetry parameter, η_Q, are nearly identical to those derived experimentally.

3.3. NLMO Analysis of ^{99}Ru EFG Tensors. The EFG tensor of a transition metal in a ligand field is determined by the distribution of charge arising from the valence d-shell and concomitant interactions with ligand frontier orbitals. Polarization of the outer core of the metal ion, electron density in the metal−ligand bonding orbitals, and partial charges in the ligands, further contribute to the EFG. However, valence d-shell contributions, along with core-polarization caused by a nonspherical d-shell electron density, tend to dominate.[49,110,111]

The relative magnitudes of the EFG tensor components and orientations of the EFG tensors in the molecular frames can be interpreted in terms of the populations of the d-shell orbitals. The data in Table 2 are based on model calculations[49] with d-orbitals that have the same radial functions, such that a filled d-shell, or a partially filled d-shell with equal occupations and a spherical electron density, produces a vanishing EFG tensor (i.e., the contributions from individual d-orbitals cancel exactly). The values indicate the relative contributions to the EFG tensor components in terms of a positive numerical constant ε. For example, the contributions from individual d-orbitals to V_{zz}, shows that they cancel if each orbital has the same occupation. Nonequal occupations typically lead to incomplete cancellation of the various positive and negative contributions and therefore to a nonzero EFG. For example, a filled d_{z^2} orbital generates $V_{zz} = -2\varepsilon$, whereas $V_{xx} = V_{yy} = +\varepsilon$. In this example, the orbital's electron density is concentrated along the orbital's principal axis (z), which leads to a negative V_{zz} based on the sign convention used here for the EFG. The data can also be interpreted as a lack of counterbalancing electron density in the xy plane with concomitant positive $V_{xx} = V_{yy}$. The relative magnitudes of the EFG tensor components are associated with how effectively the electron density (or lack thereof) accumulates with respect to the different axes or planes. The d_{xy}, d_{xz}, and d_{yz} EFG contributions follow the same rules: The lack of electron density perpendicular to the xy, xz, and yz plane, respectively, causes a $+2\varepsilon$ contribution to the EFG in the perpendicular direction, along with $-\varepsilon$ in-plane contributions.

Table 2. Relative Contributions to the Ru Cartesian EFG Tensor Components from Pure Ru 4d-Orbitals[a,b,c,d]

	d_{xy}	d_{xz}	d_{yz}	$d_{x^2-y^2}$	d_{z^2}
V_{xx}	$-\varepsilon$	$-\varepsilon$	2ε	$-\varepsilon$	ε
V_{yy}	$-\varepsilon$	2ε	$-\varepsilon$	$-\varepsilon$	ε
V_{zz}	2ε	$-\varepsilon$	$-\varepsilon$	2ε	-2ε

[a]Per the numerical analysis in the text, ε for the studied Ru complexes is approximately 2.55 a.u. [b]The EFG sign convention used here is such that a negative EFG arises when electron density (i.e., negative charge) localizes along a particular axis. [c]V_{xx}, V_{yy}, and V_{zz} define the principal values of the EFG tensors within an arbitrary Cartesian reference frame that defines the nature and labels of the d AOs. [d]The value of 2ε is equivalent to the largest principal component of the EFG tensor (either V_{33} or V_{zz}, depending on the naming convention).

Table 3 provides the localized MO analysis (in terms of NLMOs) of the ^{99}Ru EFG tensor for each complex. Polar plots of the EFG tensors[49] and the orientations of the principal axes systems relative to the molecular frames are provided in Figure 4. In the analysis, 'LP' means lone-pair, which includes the nonbonding Ru 4d orbitals, 'BD' indicates bonding orbitals, and the Ru core corresponds to [Kr]. The EFG tensors of Cp_2Ru and Cp^*_2Ru are very similar and display axial symmetry, with V_{33}, which is positive and oriented near a pseudo-D_{5h} axis in each case, being about twice the magnitude and opposite in sign compared to $V_{11} \approx V_{22}$. In an idealized D_{5h} complex, the metal EFG tensor components V_{11} and V_{22} and the associated NLMO contributions of symmetry-equivalent d-orbitals are equal. There is minor symmetry breaking in the calculated data, which reflects the structure of the complex in the solid being close to the idealized D_{5h} symmetry. For Cp*ClRu(cod), which has lower symmetry, V_{33} is negative and oriented approximately perpendicular to the Ru−Cl bond, and the EFG tensor is nonaxial (i.e., $\eta_Q = 0.75$ according to calculations and $\eta_Q = 0.76$ according to experiment).

Ru^{2+} has a d^6 valence configuration. For Cp_2Ru, the direction corresponding to the Ru − Cp-centroids was chosen to align with the z direction (i.e., $V_{33} = V_{zz}$ and $V_{11} \approx V_{22} = V_{xx}$ or V_{yy}). In the pseudolinear ligand field, the *formal* Ru electron configuration is expected to be $(d_{xy})^2(d_{xz})^0(d_{yz})^0(d_{x^2-y^2})^2(d_{z^2})^2$. Figure S5 shows occupied nonbonding d_{z^2} (***1a***) and two d-orbitals with electron density localized in the xy plane (***1b***, ***1c***), i.e., d_{xy} and $d_{x^2-y^2}$, with back-donation to the Cp ligands. The ligand does not have low-energy unoccupied orbitals of the right symmetry to accommodate back-donation from $4d_{z^2}$, and therefore its EFG contributions must correspond closely to what is expected from an atomic 4d orbital. d_{z^2} contributes −5.31 a.u. to V_{33}, while the average of the nearly equal contributions to V_{11} and V_{22} is +2.62 au (*N.B.*: all EFG values are reported in a.u.; these units are omitted hereafter for brevity). The latter is very close to −1/2 of the d_{z^2} contribution to V_{33}, as would be expected based on the idealized −2:1 ratios for V_{zz}/V_{xx} and V_{zz}/V_{yy} from pure, undistorted Ru 4d AOs (*cf.* Table 2). We may therefore assign a value of 2.65 to the constant ε.

Compared to d_{z^2}, absent back-donation, d_{xy} and $d_{x^2-y^2}$ should contribute $2\varepsilon = +5.31$ each to V_{33} in Cp_2Ru. The actual values are notably smaller (+4.79 and +4.80, respectively) because

https://doi.org/10.1021/jacs.5c04759
J. Am. Chem. Soc. 2025, 147, 20865−20877

Table 3. Major Contributions to Principal Components of ^{99}Ru EFG Tensors from NLMOs[a,b,c]

	V_{11} (a.u.)	V_{22} (a.u.)	V_{33} (a.u.)
Cp_2Ru			
Ru core	−0.725	−0.741	1.468
1a: LP(Ru)$_a$ [d_{z^2}][d]	2.660	2.648	−5.308
1b: LP(Ru)$_b$ [d_{xy}][d]	−2.393	−2.399	4.792
1c: LP(Ru)$_c$ [$d_{x^2-y^2}$][d]	−2.402	−2.398	4.800
ΣRu LP	−2.135	−2.149	4.284
Σ***1d-i:*** BD(Cpπ)→Ru	1.544	1.582	−3.126
other C−C BD	0.458	0.381	−0.838
Σabove	−0.858	−0.927	1.788
Total calc.	−0.805	−0.846	1.654
Cp^*_2Ru			
Ru core	−0.609	−0.648	1.259
2a: LP(Ru)$_a$ [d_{z^2}][d]	2.549	2.598	−5.146
2b: LP(Ru)$_b$ [d_{xy}][d]	−2.369	−2.391	4.760
2c: LP(Ru)$_c$ [$d_{x^2-y^2}$][d]	−2.366	−2.382	4.747
ΣRu LP	−2.186	−2.175	4.361
Σ***2d-i:*** BD(Cpπ)→Ru	1.509	1.517	−3.026
other C−C BD	0.528	0.525	−1.052
C−H BD	−0.148	−0.146	0.292
Σabove	−0.906	−0.927	1.834
Total calc.	−0.847	−0.866	1.716
Cp*ClRu(cod)			
Ru core	−0.142	0.594	−0.456
3a: LP(Ru)[a]	3.588	0.977	−4.566
3b: LP(Ru)[b]	−0.463	1.693	−1.230
3c: LP(Ru)[c]	−3.075	−0.100	3.174
ΣRu LP	0.050	2.570	−2.622
3d: BD(Ru−Cl)	−1.203	−0.101	1.303
3e: Ru→BD(Cpπ)	−0.960	−0.921	1.880
Σ***3f-h:*** LP(Cl)	−0.118	0.041	0.077
ΣRu LP ***3f-h:*** BD(Cpπ)→Ru	1.288	−0.561	−0.727
ΣRu LP ***3k-l:*** BD(codπ)→Ru	1.035	0.215	−1.251
Σabove	−0.050	1.837	−1.796
Total calc.	0.200	1.406	−1.610

[a]EFG data are given in dimensionless atomic units (a.u.). One a.u. of EFG corresponds to *ca.* 9.717 × 10^{17} V cm^{-2}. [b]The nuclear charge contributions to the EFG are absorbed in the NLMO analysis, such that the sum of contributions from NLMOs that are distant from the Ru center represents the EFG generated by distant partial charges. [c]In the analysis, "LP" means lone-pair, which includes the nonbonding Ru 4d orbitals, "BD" means bonding orbitals, and the Ru core corresponds to [Kr]. [d]These designations do not necessarily correspond to pure d orbitals, and are instead used to assist the reader.

some of the electron density in these orbitals is donated to the ligands. The EFG operator has an r^{-3} dependence on the distance r between the electrons and the Ru nucleus, such that the back-donation strongly reduces the contributions of d_{xy} and $d_{x^2-y^2}$ to V_{33}. Likewise, based on purely atomic 4d orbitals, we expect d_{xy} and $d_{x^2-y^2}$ to contribute approximately $-\varepsilon = -2.65$ to V_{11} and V_{22}. The actual contributions are lower (−2.40) because of the density loss in these orbitals due to back-donation. Based on the ratios of expected vs actual EFG contributions from orbitals ***1a*−*1c*** (Table 3 and Figure S5) to V_{11}, V_{22}, and V_{33}, we estimate that *ca.* 10% of the electron density in each of these orbitals is donated to the ligands. The Ru density weight percentages of NLMOs ***1a***, ***1b***, and ***1c*** were calculated as 97.5, 87.4, and 87.5, respectively. Therefore, ***1a*** is a nearly pure $4d_{z^2}$, whereas the back-donation causes the Ru

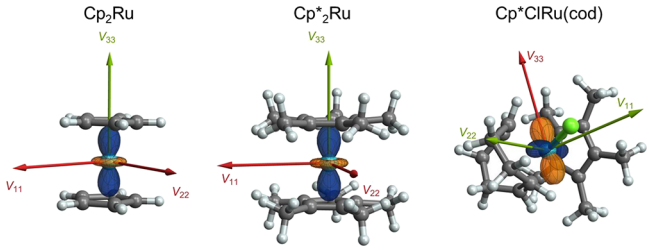

Figure 4. Polar plots of the Ru EFG tensors and Cartesian principal components superimposed on the complex. The polar plot scaling is such that a distance of the surface of 1 Å from the Ru nucleus corresponds to an EFG of 1 a.u. Blue/orange on the polar plots corresponds to a positive/negative EFG. [*N.B.*: EFG tensor polar plots resemble polar plots for atomic d-orbitals for the reason that the quadrupolar interaction is associated with $l = 2$ spherical tensors, but they should not be confused with orbital visualizations.] Arrows indicate the orientations of the principal values of the EFG tensors, with green/red corresponding to positive/negative EFGs.

density weight in the formally nonbonding $4d_{xy}$ and $4d_{x^2-y^2}$ (***1b***, ***1c***) to be lower by *ca.* 10%. We note that a nonbonding NLMO must still be orthogonal to all other NLMOs, including those centered on the ligands, which means that it cannot have 100% metal character in the analysis even when back-donation is absent.

In the localized orbital representation, the π system in one of the Cp ligands is described by three doubly occupied π NLMOs per Cp that each display delocalization around the Cp rings, as expected for a Hückel-aromatic system. Accordingly, there are six ligand-centered NLMOs for Cp_2Ru (orbitals ***1d*−*1i*** in Figure S5). The ligand orbitals donate into linear combinations of the Ru $4d_{xz}$ and $4d_{yz}$ orbitals, which appear d_{z^2}-like but tilted 45° relative to the principal axis of symmetry. Accordingly, there are considerable negative contributions from these ligand-centered orbitals to V_{33}, with signs consistent with Table 2. When d_{xz} and d_{yz} are evenly populated, the ratios V_{zz}/V_{xx} and V_{zz}/V_{yy} for the EFG generated by these Ru AOs are both −2:1, which is nearly the case for the data shown in Table 3 (i.e., we may expect an idealized $V_{zz} = -2\varepsilon = -5.31$ (rounded) from the sum of d_{xz} and d_{yz} if they were both completely filled). The actual sum of V_{33} from NLMOs ***1d*−*1i*** is −3.13, which comes from aggregate electron donation into d_{xz} and d_{yz} and the EFG generated by the partial charges in the ligands. If we ignore the latter, the ratio −3.13/−5.31 indicates that the filling of d_{xz} and d_{yz} is *ca.* 59% each on average. Using the V_{11} and V_{22} data gives a similar picture: The idealized sum $V_{11} + V_{22}$ for d_{xz} and d_{yz} is $2\varepsilon = +5.31$, whereas the actual sum of V_{11} and V_{22} from NLMOs ***1d*−*1i*** is +3.13 (rounded), equal and opposite to the sum of their contributions to V_{33}. The calculated Ru density weight percentages of NLMOs ***1d*−*1i*** (divided by two to account for the donation into both d_{xz} and d_{yz}) add up to 54%, which is reasonably close to the 59% estimate from the idealized versus actual EFG contributions of these orbitals. The difference between these values is tentatively attributed to the EFG arising from the relatively small partial charges of the atoms in the ligands.

In summary, the EFG tensor of Cp_2Ru reflects the nonspherical electron density from the formal $(d_{xy})^2(d_{xz})^0(d_{yz})^0(d_{x^2-y^2})^2(d_{z^2})^2$ configuration. In an idealized system, this would lead to EFG tensor components of (V_{xx}, V_{yy}, V_{zz}) = ($-\varepsilon$, $-\varepsilon$, $+2\varepsilon$) ≈ (−2.65, −2.65, +5.31). The actual EFG tensor has a considerably smaller magnitude for two reasons: (i) because of ligand-to-metal donation, d_{xz} and d_{yz}

https://doi.org/10.1021/jacs.5c04759
J. Am. Chem. Soc. 2025, 147, 20865−20877

are roughly half occupied each, instead of empty; and (ii) d_{xy} and $d_{x^2-y^2}$ are not fully occupied because of back-donation. Furthermore, there is considerable outer-core polarization of Ru (4sp and 3d, primarily), listed in Table 3 under 'Ru core', which reinforces the Ru 4d-shell contributions and counteracts the Cp-to-metal donation. Core contributions are not straightforward to analyze, because minute changes in the shapes or occupations of outer core orbitals cause large effects regarding the EFG, but they tend to follow the overall trends of the valence shells.[49]

For Cp^*_2Ru, the ratios of actual EFG contributions and those based on Table 2 are consistent with the amount of density from Ru/ligand-centered NLMOs that is donated to ligand/Ru acceptor orbitals (Table 3, Figure S6). The minor differences between Cp_2Ru and Cp^*_2Ru indicate a slightly different propensity of the ligands for donation and back-donation, but the differences are close to the accuracy limits of the DFT calculations and therefore not discussed in detail.

Cp*RuCl(cod) has a lower symmetry coordination environment in comparison to Cp_2Ru and Cp^*_2Ru; as such, the analysis is less straightforward in terms of how closely the Ru formally nonbonding NLMOs correspond to the standard representations of the d-orbitals and in terms of how asymmetric the bonds and ligand-centered orbitals appear (Figure S7). However, the analysis gives a set of orbitals that define how the EFG is generated from the Ru 4d shell augmented by contributions from the Ru core and the Ru-ligand bonding orbitals. The 4d NLMOs, in aggregate, generate an EFG tensor that is nonaxial and a negative V_{33} (approximately perpendicular to the Ru−Cl bond) with a significantly reduced magnitude resulting from ligand donation and back-donation. Therefore, the general trends are the same as for Cp_2Ru and Cp^*_2Ru: (i) a large EFG is generated by the nonspherical 4d electron density coupled with core-polarization contributions; (ii) the 4d-shell EFG is reduced by donation into the formally empty 4d atomic orbitals; and (iii) the EFG is further reduced by back-donation of density from the formally nonbonding occupied 4d orbitals to the ligands.

3.4. NLMO Analysis of ^{99}Ru Chemical Shift Tensors.

The shielding analysis was performed using the same set of NLMOs as in the EFG analysis, and therefore the same considerations regarding the extent of donation and back-donation impacting the orbitals apply. We use an orbital 'rotation' model[112] for d-orbitals:[59] when a d-AO in the standard representation (d_{xy}, d_{xz}, d_{yz}, $d_{x^2-y^2}$, d_{z^2}) is perturbed by a static magnetic field along one of the Cartesian axes, the resulting perturbation is in first order proportional to the AO rotated by either 45° or 90°, depending on which d-AO and which field direction. For example, a magnetic field applied along the z-axis is described quantum mechanically by an operator $\hat{B}_z$ that is approximately proportional to the angular momentum operator $-i\hbar[\boldsymbol{r} \times \nabla]_z$ for a rotation around z. Taking only the $[\boldsymbol{r} \times \nabla]_z$ part of this operator, its action on, say, a d_{xy} AO 'rotates' the AO 45° in the xy-plane such that the lobes align with the x- and y-axes (Scheme 2).[113]

When applied to a nonbonding occupied 4d AO (or a corresponding NLMO), such a 'rotation' may result in efficient overlap with a low-energy unoccupied orbital, typically in the form of a σ^* from a coordinating ligand. Stated differently, the paramagnetic component of the shielding tensor affords sizable matrix elements such as $\langle \sigma^*_{x \text{ or } y} | \hat{B}_z | d_{xy} \rangle$, where the subscript of the σ^* orbital indicates its directionality. Such a d-σ^* magnetic coupling results in deshielding, which is large when the magnetically coupled orbitals are close in energy, and when matrix elements of the type shown above are large; the latter is the case when field-'rotated' occupied orbitals overlap effectively with unoccupied orbitals. Analogously to the EFG contributions, the shielding contribution from a given metal AO is modulated by the degree of donation or back-donation that is present.

Scheme 2. Action of the Angular Momentum Operator Components on d-AOs, Leading to "Rotated" d-AOs; Figure Adapted from Ref 113 with Permission, Copyright 2024 Royal Society of Chemistry

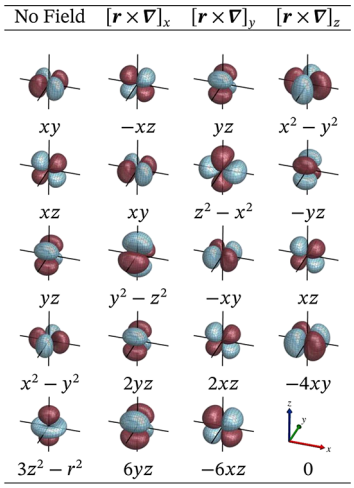

Table 4 summarizes the shielding tensor analysis. Polar plots of the magnetic shielding tensor and the orientation of the principal axis system relative to the molecular frame are provided in Figure 5. The total shielding is largely a sum of (diamagnetic) shielding from the electrons in the Ru core and the (mainly paramagnetic) deshielding from the partially occupied 4d shell. The analysis of the paramagnetic shielding includes SO effects, which are not listed separately. Additionally, the analysis of the SO-ZORA shielding tensor in terms of SR NLMOs includes contributions from unoccupied NLMOs, which reflect the SO-induced changes of the occupied ground state orbitals. These contributions make up most of the difference between the sum of the listed individual shielding contributions and the total calculated shielding tensor components. Differences in SO contributions between complexes are comparatively small and not discussed.

In terms of the formally nonbonding orbitals of the 4d shell in Cp_2Ru, d_{z^2} (orbital ***1a*** in Figure S5) contributes strongly to σ_{11} and σ_{22} via the paramagnetic 4d shell effect, but negligibly to σ_{33}. This is because the perturbation of d_{z^2} by a static magnetic field along the z-axis effectively vanishes, whereas fields in the x or y directions produce from d_{z^2} perturbations resembling d_{yz} and d_{xz}, respectively (see Scheme 2; also recall that d_{yz} and d_{xz} in this complex are formally empty). Therefore, the perturbation of d_{z^2} by a magnetic field in the x or y direction and the availability of mostly unoccupied d_{yz} and d_{xz} (***1j***, ***1k*** in Figure S8) provides a pathway for strong paramagnetic deshielding originating from d_{z^2}. The partial occupations of d_{yz} and d_{xz} via ligand donation reduce the magnitude of the d_{z^2} deshielding for a field in the x or y direction.

Contributions from nonbonding orbitals d_{xy} (***1b***) and $d_{x^2-y^2}$ (***1c***) to the Cp_2Ru shielding are more isotropic. For both of these lone-pairs, a magnetic field in the equatorial plane (x or

https://doi.org/10.1021/jacs.5c04759
J. Am. Chem. Soc. 2025, 147, 20865−20877

Table 4. Major Contributions to Principal Components of ^{99}Ru Magnetic Shielding Tensors from NLMOs[a,b]

	σ_{11} (ppm)	σ_{22} (ppm)	σ_{33} (ppm)
Cp_2Ru			
Ru core	3991	3991	4053
1a: LP(Ru)$_a$ [d_{z^2}][c]	−3692	−3683	44
1b: LP(Ru)$_b$ [d_{xy}][c]	−539	−606	−426
1c: LP(Ru)$_c$ [$d_{x^2-y^2}$][c]	−572	−576	−430
ΣRu LP	−4802	−4865	−812
Σ***1d-i:*** BD(Cpπ)→Ru	630	674	345
other C−C BD	87	120	−43
Σabove	−94	−80	3543
Total calc.	−147	−130	3538
Cp^*_2Ru			
Ru core	4107	4106	4129
2a: LP(Ru)$_a$ [d_{z^2}][c]	−3641	−3611	41
2b: LP(Ru)$_b$ [d_{xy}][c]	−693	−709	−652
2c: LP(Ru)$_c$ [$d_{x^2-y^2}$][c]	−702	−696	−650
ΣRu LP	−5037	−5016	−1261
Σ***2d-i:*** BD(Cpπ)→Ru	416	420	176
other C−C BD	85	80	−52
C−H BD	−188	−182	−152
Σabove	−617	−593	2839
Total calc.	−655	−631	2836
Cp*ClRu(cod)			
Ru core	4242	4241	4199
3a: LP(Ru)[a]	−5095	−548	−906
3b: LP(Ru)[b]	−235	−1295	−2446
3c: LP(Ru)[c]	−794	−3086	−770
ΣRu LP	−6124	−4928	−4122
3d: BD(Ru−Cl)	−55	−31	3
3e: Ru→BD(Cpπ)	15	−105	18
Σ***3f-h:*** LP(Cl)	−21	−30	−33
ΣRu LP ***3f-h:*** BD(Cpπ)→Ru	209	−90	−24
ΣRu LP ***3k-l:*** BD(codπ)→Ru	−309	153	−31
Σabove	−2044	−790	11
Total calc.	−2270	−977	−139

[a]The analysis of the paramagnetic shielding includes SO effects, which are not listed separately. [b]In the analysis, "LP" means lone-pair, which includes the nonbonding Ru 4d orbitals, "BD" means bonding orbitals, and the Ru core corresponds to [Kr]. [c]These designations do not necessarily correspond to pure d orbitals, and are instead used to assist the reader.

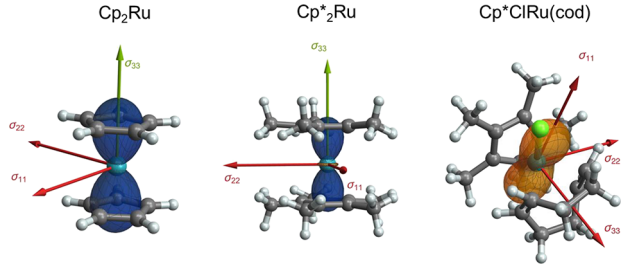

Figure 5. Polar plots of the Ru magnetic shielding tensors and Cartesian principal components superimposed on the complex. The polar plot scaling is such that a distance of the surface of 1 Å from the Ru nucleus corresponds to a shielding value of 1000 ppm. Blue/orange on the polar plots corresponds to a positive/negative shielding. Arrows indicate the orientations of the principal axes of the chemical shift tensors, with green/red corresponding to a positive/negative principal shielding component.

y) gives a function resembling d_{xz} or d_{yz} but with smaller coefficients than in the case of d_{z^2}. With the magnetic field in the z direction, 'rotation' of d_{xy} ($d_{x^2-y^2}$) gives a function resembling $d_{x^2-y^2}$ (d_{xy}). The only unoccupied orbitals of matching symmetry are the same π^* ligand combinations that receive back-donation from d_{xy} and $d_{x^2-y^2}$, respectively (***1l***, ***1m***, ***1n***, ***1o*** in Figure S8). In other words, the occupied Ru-centered MOs ***1b*** and ***1c***, which form in-phase linear combinations with the ligand π^* MOs, are accompanied by the unoccupied out-of-phase counterparts available for magnetic coupling when the field is in the z direction. However, the latter orbitals are mainly ligand-centered with comparatively small coefficients from Ru AOs; hence, the shielding contributions are smaller than those found for d_{z^2} and fields in the x or y direction. For all field directions, a deshielding effect is generated by ***1b*** and ***1c*** with roughly equal contributions.

In contrast to the EFGs, the shielding tensors of Cp_2Ru and Cp^*_2Ru are not as similar. In Cp^*_2Ru, σ_{11} and σ_{22} are more negative by over 500 ppm, and σ_{33} is less positive by over 700 ppm. About 200 ppm of the difference in σ_{11} and σ_{22}, and about 400 ppm for σ_{33}, is attributed to differences in the contributions from the Ru 4d shell, namely orbitals ***1b***/***2b*** and ***1c***/***2c***. It can be inferred from the minor differences in their EFG contributions that there is not a significant difference in the degree of donation or back-donation that would drive the differences between Cp_2Ru and Cp^*_2Ru in the shielding contributions from the 4d orbitals. This is substantiated by the explicitly calculated occupations for the corresponding NBOs, which are 1.76 (***1b*** and ***1c***) and 1.77 (***2b*** and ***2c***).

Differences between Cp_2Ru and Cp^*_2Ru are seen in the Ru (outer) core contributions which are overall more positive for Cp*, and the d_{xy} and $d_{x^2-y^2}$ contributions (***2b***, ***2c***) which are more negative for Cp*. Additionally, differences in the donating orbital contributions (***1d−1i*** in Figure S5 vs ***2d−2i*** in Figure S6) are less positive for Cp*. Overall, all three shielding tensor components are more negative/less positive for Cp* than Cp. The positive sign of the Ru shielding from the donating orbitals is attributed to the aforementioned fact that donation into d_{xz} and d_{yz} means these mostly vacant AOs are not fully available for the paramagnetic coupling within the 4d shell. As to the differences in the shielding from the occupied donating π NLMOs, the unoccupied antibonding counterparts have noticeably higher energies for Cp^*_2Ru (Figure S9), which is expected to translate into less shielding.

There is also the question of how much shielding from ligand-centered π orbitals (***1d−1i*** for the Cp complex) is attributable to magnetic field-induced ring currents. Calculations were performed to obtain the presence of a nucleus-independent chemical shift (NICS) for Cp^- or Cp^{*-} and the NMR shielding was calculated for a dummy atom placed at a relative position where Ru is present in the complexes. The results for (σ_{11}, σ_{22}, σ_{33}) for Cp^- and Cp^{*-} are (−1.9, −1.8, 25.9) and (−1.3, −1.2, 17.4), respectively; this indicates that there is an induced ring-current effect mainly for the field in the z direction, but the effect is small.

The contributions of the NLMOs to ruthenium shielding in Cp*ClRu(cod) are cumbersome to interpret, due in part to its low symmetry. A few points of analysis can be made: (i) the deshielding from the 4d shell dominates the shielding from the Ru core, such that the total shielding is negative for each principal component; (ii) LP orbital ***3a*** contributes a large deshielding in the σ_{11} direction; (iii) LP orbital ***3b*** contributes its largest deshielding effect for the field in the σ_{33} direction,

https://doi.org/10.1021/jacs.5c04759
J. Am. Chem. Soc. 2025, 147, 20865−20877

and **3c** contributes its largest deshielding effect for the field in the σ_{22} direction; and (iv) contributions from ligand-centered orbitals are minimal.

CONCLUSIONS

Herein, we have highlighted the use of ^{99}Ru SSNMR spectroscopy and relativistic DFT calculations as a powerful means of characterizing ruthenium organometallic compounds, with the ^{99}Ru EFG and chemical shift tensors being robust probes of Ru-ligand bonding. The WURST-QCPMG pulse sequence, which affords broadband excitation and refocusing, while also allowing for T_2-based signal enhancement, is invaluable for the acquisition of high signal-to-noise ^{99}Ru ultrawideline SSNMR powder patterns. Similarly, the BRAIN-CP pulse sequence allows for broadband polarization transfer from abundant spins, and could potentially allow such ultrawideline patterns to be obtained in more reasonable timeframes (and enable more routine exploration with ^{1}H−^{99}Ru dynamic nuclear polarization NMR). Furthermore, access to high magnetic fields (i.e., up to 36 T) proves critical for the acquisition of ^{99}Ru powder patterns, as well as for the ability to accurately extract EFG and chemical shift tensors. Together, these advanced experimental methods and access to GHz-class NMR magnets have the potential to aid in the characterization of a plethora of Ru coordination compounds, and will likely find applications to the study of other PGEs (e.g.,^{103}Rh,^{105}Pd) and other transition metal nuclides.

Quantum chemical calculations using DFT and a relativistic Hamiltonian provide the crucial link between ^{99}Ru NMR interaction tensors and the nature of ruthenium-ligand bonding. We find the best agreement with experiment through the following considerations: (i) relativistic effects are included up to the spin−orbit level, and (ii) a hybrid DFT functional is used, with attention paid to the optimal admixture of eX. Following this, the origins of EFG and chemical shift tensors can be analyzed in terms of contributions from relevant NLMOs and/or NBOs (or other sets of localized MOs), leading to an understanding of how the chemical bonding and in particular the donation to the metal, and back-donation from the metal, manifest in corresponding SSNMR spectra. Such analyses will be critical for studying bonding in a variety of PGE coordination compounds (from the perspective of both metal and ligand nuclei), including the establishment of structure-property-function relationships, and may aid the search for novel advanced materials with tunable physico-chemical properties.

ASSOCIATED CONTENT

Supporting Information

The Supporting Information is available free of charge at https://pubs.acs.org/doi/10.1021/jacs.5c04759.

Powder X-ray diffractograms, experimental details and acquisition parameters, additional DFT calculations, and molecular orbital isosurfaces (PDF)

AUTHOR INFORMATION

Corresponding Authors

Jochen Autschbach − *Department of Chemistry, State University of New York at Buffalo, Buffalo, New York 14260, United States;* orcid.org/0000-0001-9392-877X; Email: jochena@buffalo.edu

Robert W. Schurko − *Department of Chemistry & Biochemistry, Florida State University, Tallahassee, Florida 32306, United States; National High Magnetic Field Laboratory, Tallahassee, Florida 32310, United States;* orcid.org/0000-0002-5093-400X; Email: rschurko@fsu.edu

Authors

Sean T. Holmes − *Department of Chemistry & Biochemistry, Florida State University, Tallahassee, Florida 32306, United States; National High Magnetic Field Laboratory, Tallahassee, Florida 32310, United States;* orcid.org/0000-0002-5821-9641

Yijue Xu − *National High Magnetic Field Laboratory, Tallahassee, Florida 32310, United States*

Adam B. Philips − *Department of Chemistry, State University of New York at Buffalo, Buffalo, New York 14260, United States;* orcid.org/0000-0002-5742-6817

Sara Termos − *Department of Chemistry & Biochemistry, Florida State University, Tallahassee, Florida 32306, United States; National High Magnetic Field Laboratory, Tallahassee, Florida 32310, United States*

James J. Kimball − *Department of Chemistry & Biochemistry, Florida State University, Tallahassee, Florida 32306, United States; National High Magnetic Field Laboratory, Tallahassee, Florida 32310, United States;* orcid.org/0000-0002-4993-6892

Complete contact information is available at: https://pubs.acs.org/10.1021/jacs.5c04759

Notes

The authors declare no competing financial interest.

ACKNOWLEDGMENTS

This material is based upon work supported by the U.S. Department of Energy, Office of Science, Office of Basic Energy Sciences, under Award Number DE-SC0022310. This funding covered expenses associated with project personnel, chemicals, and consumable materials. We are also grateful for support from The Florida State University and the National High Magnetic Field Laboratory (NHMFL), which is funded by the National Science Foundation Cooperative Agreement (DMR-1644779 and DMR-2128556) and the State of Florida. We thank Peter Gor'kov, Jason Kitchen, and Wenping Mao for their work on low-γ probe configurations, as supported by the National Resource for Advanced NMR Technology (NIH RM1 GM148766), as well as the design of airtight sample containers. J.A. and A.B.P. thank the Center for Computational Research at U. Buffalo for providing computing resources (http://hdl.handle.net/10477/79221). A portion of this research used resources provided by the X-ray Crystallography Center at the FSU Department of Chemistry & Biochemistry (FSU075000XRAY).

REFERENCES

(1) Rao, C. R. M.; Reddi, G. S. Platinum group metals (PGM); occurrence, use and recent trends in their determination. *Trends Anal. Chem.* **2000**, *19*, 565−586.

(2) Hartley, F. R.*Chemistry of the Platinum Group Metals*; Elsevier Science Publishers B.V. 1991

(3) *Critical Minerals and Materials - U.S. DOE's Strategy to Support Domestic Critical Mineral and Material Supply Chains (FY 2021−FY 2031)*. U.S. Department of Energy, Ed.; Washington, D.C., 2020.

(4) *Mineral Commodity Summaries 2024* Survey, U. S. G., Ed.; Reston, VA, 2024.
(5) ElGuindy, M.Platinum Group Metals: Alloying, Properties, and Applications. In *Encyclopedia of Materials: Science and Technology*, Buschow, K. H. J.; Cahn, R. W.; Flemings, M. C.; Ilschner, B.; Kramer, E. J.; Mahajan, S.; Veyssière, P., Eds.; Elsevier, 2001; pp 7117−7121.
(6) Zientek, M. L.; Loferski, P. J. *Platinum-group elements: So many excellent properties*; U.S. Geological Survey: Reston, VA, 2014. https://pubs.usgs.gov/publication/fs20143064 .
(7) Nassar, N. T. Limitations to elemental substitution as exemplified by the platinum-group metals. *Green Chem.* **2015**, *17*, 2226−2235.
(8) Obeng, A.; Autschbach, J. How much electron donation is there in transition metal complexes? a computational study. *J. Chem. Theory Comput.* **2024**, *20*, 4965−4976.
(9) Hansen, J. H.; Parr, B. T.; Pelphrey, P.; Jin, Q.; Autschbach, J.; Davies, H. M. L. Rhodium(II)-catalyzed cross-coupling of diazo compounds. *Angew. Chem., Int. Ed.* **2011**, *50*, 2544−2548.
(10) Holmes, S. T.; Schönzart, J.; Philips, A. B.; Kimball, J. J.; Termos, S.; Altenhof, A. R.; Xu, Y.; O'Keefe, C. A.; Autschbach, J.; Schurko, R. W. Structure and bonding in rhodium coordination compounds: a ^{103}Rh solid-state NMR and relativistic DFT study. *Chem. Sci.* **2024**, *15*, 2181−2196.
(11) Harris, R. K.; Becker, E. D.; Cabral De Menezes, S. M.; Goodfellow, R.; Granger, P. NMR nomenclature: nuclear spin properties and conventions for chemical shifts (IUPAC recommendations 2001). *Concepts Magn. Reson.* **2002**, *14*, 326−346.
(12) Ishida, K.; Kawasaki, Y.; Kitaoka, Y.; Asayama, K.; Nakamura, H.; Flouquet, J. Ru NMR and NQR probes of the metamagnetic transition in $CeRu_2Si_2$. *Phys. Rev. B* **1998**, *57*, R11054−R11057.
(13) Mukuda, H.; Ishida, K.; Kitaoka, Y.; Asayama, K.; Kanno, R.; Takano, M. Spin fluctuations in the ruthenium oxides RuO_2, $SrRuO_3$, $CaRuO_3$, and Sr_2RuO_4 probed by Ru NMR. *Phys. Rev. B* **1999**, *60*, 12279−12285.
(14) Sakai, H.; Osawa, N.; Yoshimura, K.; Fang, M.; Kosuge, K. ^{99,101}Ru NMR study of $EuSr_2Cu_2O_8$: coexistence of ferromagnetism and superconductivity. *Phys. Rev. B* **2003**, *67*, No. 184409.
(15) Han, Z. H.; Budnick, J. I.; Hines, W. A.; Dabrowski, B.; Maxwell, T. Nuclear magnetic resonance study of the Ru/Mn valence states and magnetic interactions in $SrRu_{0.9}Mn_{0.1O3}$. *Appl. Phys. Lett.* **2006**, *89*, 102501.
(16) Sakai, H.; Yoshimura, K.; Kato, H.; Kambe, S.; Walstedt, R. E. NMR study of metallic pyrochlore ruthenium oxides, $Bi_2Ru_2O_7$ and $Pb_2Ru_2O_{7-\delta}$. *J. Phys. Chem. Solids* **2002**, *63*, 1039−1041.
(17) Furukawa, Y.; Takada, S.; Kumagai, K.; Kawashima, T.; Takayama-Muromachi, E.; Kobayashi, N.; Fukase, T.; Chiba, K.; Goto, T. NMR studies of magnetic superconductor $RuSr_2RECu_2O_8$ (RE = Gd, Eu and Y). *J. Phys. Chem. Solids* **2002**, *63*, 2315−2318.
(18) Sakai, H.; Osawa, N.; Yoshimura, K.; Fang, M.; Kosuge, K. ^{99,101}Ru NMR study of $EuSr_2RuCu_2O_8$. *Physica C* **2002**, *378*−*381*, 399−403.
(19) Ooms, K. J.; Wasylishen, R. E. Solid-state Ru-99 NMR spectroscopy: a useful tool for characterizing prototypal diamagnetic ruthenium compounds. *J. Am. Chem. Soc.* **2004**, *126*, 10972−10980.
(20) Kupce, E.; Freeman, R. Optimized adiabatic pulses for wideband spin onversion. *J. Magn. Reson.* **1996**, *118*, 299−303.
(21) Schurko, R. W. Ultra-wideline solid-state NMR spectroscopy. *Acc. Chem. Res.* **2013**, *46*, 1985−1995.
(22) Schurko, R. W.; Harris, R. K. Acquisition of wideline solid-state NMR spectra of quadrupolar nuclei. *NMR Quadrupolar Nucl. Solid Mater.* **2007**, 77−93.
(23) O'Dell, L. A. The WURST kind of pulses in solid-state NMR. *Solid State Nucl. Magn. Reson.* **2013**, *55*−*56*, 28−41.
(24) Carr, H. Y.; Purcell, E. M. Effects of diffusion on free precession in nuclear magnetic resonance experiments. *Phys. Rev.* **1954**, *94*, 630−638.
(25) Meiboom, S.; Gill, D. Modified spin-echo method for measuring nuclear relaxation times. *Rev. Sci. Instrum.* **1958**, *29*, 688−691.
(26) Larsen, F. H.; Jakobsen, H. J.; Ellis, P. D.; Nielsen, N. C. QCPMG-MAS NMR of half-integer quadrupolar nuclei. *J. Magn. Reson.* **1998**, *131*, 144−147.
(27) O'Dell, L. A.; Rossini, A. J.; Schurko, R. W. Acquisition of ultra-wideline NMR spectra from quadrupolar nuclei by frequency stepped WURST−QCPMG. *Chem. Phys. Lett.* **2009**, *468*, 330−335.
(28) O'Dell, L. A.; Schurko, R. W. QCPMG using adiabatic pulses for faster acquisition of ultra-wideline NMR spectra. *Chem. Phys. Lett.* **2008**, *464*, 97−102.
(29) Harris, K. J.; Lupulescu, A.; Lucier, B. E. G.; Frydman, L.; Schurko, R. W. Broadband adiabatic inversion pulses for cross polarization in wideline solid-state NMR spectroscopy. *J. Magn. Reson.* **2012**, *224*, 38−47.
(30) Harris, K. J.; Veinberg, S. L.; Mireault, C. R.; Lupulescu, A.; Frydman, L.; Schurko, R. W. Rapid acquisition of ^{14}N solid-state NMR spectra with broadband cross polarization. *Chem. - Eur. J.* **2013**, *19*, 16469−16475.
(31) Altenhof, A. R.; Jaroszewicz, M. J.; Harris, K. J.; Schurko, R. W. Broadband adiabatic inversion experiments for the measurement of longitudinal relaxation time constants. *J. Chem. Phys.* **2021**, *154*, No. 034202.
(32) Kimball, J. J.; Altenhof, A. A.; Jaroszewicz, M. J.; Schurko, R. W. Broadband cross polarization to half-integer quadrupolar nuclei: wideline static NMR spectroscopy. *J. Phys. Chem. A* **2023**, *127*, 9621−9634.
(33) Vega, A. J. MAS NMR spin locking of half-integer quadrupolar nuclei. *J. Magn. Reson.* **1992**, *96*, 50−68.
(34) Ashbrook, S. E.; Wimperis, S. Spin-locking of half-integer quadrupolar nuclei in nuclear magnetic resonance of solids: creation and evolution of coherences. *J. Chem. Phys.* **2004**, *120*, 2719−2731.
(35) Ashbrook, S. E.; Wimperis, S. Spin-locking of half-integer quadrupolar nuclei in nuclear magnetic resonance of solids: second-order quadrupolar and resonance offset effects. *J. Chem. Phys.* **2009**, *131*, 194509.
(36) Gan, Z.; Hung, I.; Wang, X.; Paulino, J.; Wu, G.; Litvak, I. M.; Gor'kov, P. L.; Brey, W. W.; Lendi, P.; Schiano, J. L.; et al. NMR spectroscopy up to 35.2 T using a series-connected hybrid magnet. *J. Magn. Reson.* **2017**, *284*, 125−136.
(37) Wikus, P.; Frantz, W.; Kümmerle, R.; Vonlanthen, P. Commercial gigahertz-class NMR magnets. *Supercond. Sci. Technol.* **2022**, *35*, No. 033001.
(38) Transue, W. J.; Dai, Y.; Riu, M.-L. Y.; Wu, G.; Cummins, C. C. ^{31}P NMR chemical shift tensors: windows into ruthenium phosphinidene complex electronic structures. *Inorg. Chem.* **2021**, *60*, 9254−9258.
(39) Mastrorilli, P.; Todisco, S.; Bagno, A.; Gallo, V.; Latronico, M.; Fortuño, C.; Gudat, D. Multinuclear solid-state NMR and DFT studies on phosphanido-bridged diplatinum complexes. *Inorg. Chem.* **2015**, *54*, 5855−5863.
(40) Todisco, S.; Saielli, G.; Gallo, V.; Latronico, M.; Rizzuti, A.; Mastrorilli, P. ^{31}P and ^{195}Pt solid-state NMR and DFT studies on platinum(i) and platinum(ii) complexes. *Dalton Trans.* **2018**, *47*, 8884−8891.
(41) Bernard, G. M.; Feindel, K. W.; Wasylishen, R. E.; Cameron, T. S. Solid-state phosphorus-31 NMR spectroscopy of a multiple-spin system: an investigation of a rhodium−triphosphine complex. *Phys. Chem. Chem. Phys.* **2008**, *10*, 5552−5563.
(42) Truflandier, L. A.; Autschbach, J. Probing the solvent shell with ^{195}Pt chemical shifts: density functional theory molecular dynamics study of Pt^{II} and Pt^{IV} anionic complexes in aqueous solution. *J. Am. Chem. Soc.* **2010**, *132*, 3472−3483.
(43) Truflandier, L. A.; Sutter, K.; Autschbach, J. Solvent effects and dynamic averaging of ^{195}Pt NMR shielding in cisplatin derivatives. *Inorg. Chem.* **2011**, *50*, 1723−1732.
(44) Autschbach, J.; Zheng, S. Density functional computations of ^{99}Ru chemical shifts: relativistic effects, influence of the density

https://doi.org/10.1021/jacs.5c04759
J. Am. Chem. Soc. 2025, 147, 20865−20877

functional, and study of solvent effects on *fac*—$[Ru(CO)_3I_3]^-$. *Magn. Reson. Chem.* **2006**, *44*, 989−1007.
(45) Bagno, A.; Bonchio, M. Relativistic DFT calculation of ^{99}Ru NMR parameters: chemical shifts and spin−spin coupling constants. *Magn. Reson. Chem.* **2004**, *42*, S79−S87.
(46) Bagno, A.; Bonchio, M. DFT calculations of ^{99}Ru chemical shifts with all-electron and effective core potential basis sets. *Eur. J. Inorg. Chem.* **2002**, *2002*, 1475−1483.
(47) Bühl, M.; Gaemers, S.; Elsevier, C. J. Density-functional computation of ^{99}Ru NMR parameters. *Chem. - Eur. J.* **2000**, *6*, 3272−3280.
(48) Hratchian, H. P.; Milletti, M. C. First principles determination of ^{99}Ru chemical shifts using moderately sized basis sets. *J. Mol. Struct.: THEOCHEM* **2005**, *724*, 45−52.
(49) Autschbach, J.; Zheng, S.; Schurko, R. W. Analysis of electric field gradient tensors at quadrupolar nuclei in common structural motifs. *Concepts Magn. Reson. A* **2010**, *36A*, 84−126.
(50) Alkan, F.; Dybowski, C. Calculation of chemical-shift tensors of heavy nuclei: a DFT/ZORA investigation of ^{199}Hg chemical-shift tensors in solids, and the effects of cluster size and electronic-state approximations. *Phys. Chem. Chem. Phys.* **2014**, *16*, 14298−14308.
(51) Alkan, F.; Dybowski, C. Chemical-shift tensors of heavy nuclei in network solids: a DFT/ZORA investigation of ^{207}Pb chemical-shift tensors using the bond-valence method. *Phys. Chem. Chem. Phys.* **2015**, *17*, 25014−25026.
(52) Alkan, F.; Dybowski, C. Effect of co-ordination chemistry and oxidation state on the ^{207}Pb magnetic-shielding tensor: a DFT/ZORA investigation. *J. Phys. Chem. A* **2016**, *120*, 161−168.
(53) Alkan, F.; Holmes, S. T.; Iuliucci, R. J.; Mueller, K. T.; Dybowski, C. Spin-orbit effects on the ^{119}Sn magnetic-shielding tensor in solids: a ZORA/DFT investigation. *Phys. Chem. Chem. Phys.* **2016**, *18*, 18914−18922.
(54) Alkan, F.; Dybowski, C. Spin-orbit effects on the ^{125}Te magnetic-shielding tensor: a cluster-based ZORA/DFT investigation. *Solid State Nucl. Magn. Reson.* **2018**, *95*, 6−11.
(55) Holmes, S. T.; Schurko, R. W. A DFT/ZORA study of cadmium magnetic shielding tensors: analysis of relativistic effects and electronic-state approximations. *J. Chem. Theory Comput.* **2019**, *15*, 1785−1797.
(56) Alkan, F.; Holmes, S. T.; Dybowski, C. Role of exact exchange and relativistic approximations in calculating ^{19}F magnetic shielding in solids using a cluster *ansatz*. *J. Chem. Theory Comput.* **2017**, *13*, 4741−4752.
(57) Widdifield, C. M.; Schurko, R. W. Understanding chemical shielding tensors using group theory, MO analysis, and modern density-functional theory. *Concepts Magn. Reson., Part A* **2009**, *34A*, 91−123.
(58) Fernández−Alarcón, A.; Autschbach, J. Relativistic density functional NMR tensors analyzed with spin-free localized molecular orbitals. *ChemPhysChem* **2023**, *24*, No. e202200667.
(59) Autschbach, J.; Zheng, S. Analyzing Pt chemical shifts calculated from relativistic density functional theory using localized orbitals: The role of Pt 5d lone pairs. *Magn. Reson. Chem.* **2008**, *46*, S45−S55.
(60) Autschbach, J. Analyzing NMR shielding tensors calculated with two-component relativistic methods using spin-free localized molecular orbitals. *J. Chem. Phys.* **2008**, *128*, 164112.
(61) Miyamoto, Y.; Takamizawa, S. Deformation twinning of ferrocene crystals assisted by the rotational mobility of cyclopentadienyl rings. *Dalton Trans.* **2015**, *44*, 5688−5691.
(62) Zanin, I. E.; Antipin, M. Y. Molecular and crystal structures of decamethylruthenocene $(\eta^5\text{-}C_5Me_5)_2Ru$ in the temperature range 153−300 K: thermal motion in a crystal according to X-ray diffraction data. *Crystallogr. Rep.* **2003**, *48*, 249−258.
(63) Serron, S. A.; Luo, L.; Li, C.; Cucullu, M. E.; Stevens, E. D.; Nolan, S. P. Enthalpies of reaction of Cp'Ru(COD)Cl (Cp' = C_5H_5, C_5Me_5; COD = cyclooctadiene) with $P(p\text{-}XC_6H_4)_3$ (X = Cl, F, H, CH_3, CF_3, OCH_3) ligands: ligand steric vs electronic contributions to the enthalpy of reaction. *Organometallics* **1995**, *14*, 5290−5297.
(64) Demco, D. E.; Tegenfeldt, J.; Waugh, J. S. Dynamics of cross relaxation in nuclear magnetic double resonance. *Phys. Rev. B* **1975**, *11*, 4133−4151.
(65) Pines, A.; Gibby, M. G.; Waugh, J. S. Proton-enhanced NMR of dilute spins in solids. *J. Chem. Phys.* **1973**, *11*, 569−590.
(66) Penner, G. H.; Li, W. A standard for silver CP/MAS experiments. *Solid State Nucl. Magn. Reson.* **2003**, *23*, 168−173.
(67) Larsen, F. H.; Jakobsen, H. J.; Ellis, P. D.; Nielsen, N. C. Sensitivity-enhanced quadrupolar-echo NMR of half-Integer quadrupolar nuclei. magnitudes and relative orientation of chemical shielding and quadrupolar coupling tensors. *J. Phys. Chem. A* **1997**, *101*, 8597−8606.
(68) Tegenfeldt, J.; Haeberlen, U. Cross polarization in solids with flip-back of *I*-spin magnetization. *J. Magn. Reson.* **1979**, *36*, 453−457.
(69) Lipton, A. S.; Sears, J. A.; Ellis, P. D. A general strategy for the NMR observation of half-integer quadrupolar nuclei in dilute environments. *J. Magn. Reson.* **2001**, *151*, 48−59.
(70) van Meerten, S. G. J.; Franssen, W. M. J.; Kentgens, A. P. M. ssNake: a cross-platform open-source NMR data processing and fitting application. *J. Magn. Reson.* **2019**, *301*, 56−66.
(71) Eichele, K. *WSOLIDS1: Solid-State NMR Simulation (Version 1.21.7)*; Universität Tübingen, 2021.
(72) Clark, S. J.; Segall, M. D.; Pickard, C. J.; Hasnip, P. J.; Probert, M. J.; Refson, K.; Payne, M. C. First principles methods using CASTEP. *Z. Kristallogr.* **2005**, *220*, 567−570.
(73) Pfrommer, B. G.; Côté, M.; Louie, S. G.; Cohen, M. L. Relaxation of crystals with the quasi-Newton method. *J. Comput. Phys.* **1997**, *131*, 233−240.
(74) Perdew, J. P.; Burke, K.; Ernzerhof, M. Generalized gradient approximation made simple. *Phys. Rev. Lett.* **1996**, *77*, 3865−3868.
(75) Monkhorst, H. J.; Pack, J. D. Special points for Brillouin-zone integrations. *Phys. Rev. B* **1976**, *13*, 5188−5192.
(76) Vanderbilt, D. Soft self-consistent pseudopotentials in a generalized eigenvalue formalism. *Phys. Rev. B* **1990**, *41*, 7892−7895.
(77) Tkatchenko, A.; DiStasio, R. A.; Car, R.; Scheffler, M. Accurate and efficient method for many-body van der Waals interactions. *Phys. Rev. Lett.* **2012**, *108*, No. 236402.
(78) *ADF 2021.1*; SCM, Theoretical Chemistry: Vrije Universiteit: Amsterdam, The Netherlands, 2021.
(79) Baerends, E. J.; Aguirre, N. F.; Austin, N. D.; Autschbach, J.; Bickelhaupt, F. M.; Bulo, R.; Cappelli, C.; van Duin, A. C. T.; Egidi, F.; Fonseca Guerra, C.; Forster, A.; Franchini, M.; Goumans, T. P. M.; Heine, T.; Hellstrom, M.; Jacob, C. R.; Jensen, L.; Krykunov, M.; van Lenthe, E.; Michalak, A.; Mitoraj, M. M.; Neugebauer, J.; Nicu, V. P.; Philipsen, P.; Ramanantoanina, H.; Ruger, R.; Schreckenbach, G.; Stener, M.; Swart, M.; Thijssen, J. M.; Trnka, T.; Visscher, L.; Yakovlev, A.; van Gisbergen, S. The Amsterdam Modeling Suite. *J. Chem. Phys.* **2025**, *162*, 162501.
(80) van Lenthe, E.; Jan Baerends, E. Density functional calculations of nuclear quadrupole coupling constants in the zero-order regular approximation for relativistic effects. *J. Chem. Phys.* **2000**, *112*, 8279−8292.
(81) Ditchfield, R. Self-consistent perturbation theory of diamagnetism. *Mol. Phys.* **1974**, *27*, 789−807.
(82) Wolinski, K.; Hinton, J. F.; Pulay, P. Efficient implementation of the gauge-independent atomic orbital method for NMR chemical shift calculations. *J. Am. Chem. Soc.* **1990**, *112*, 8251−8260.
(83) Rodriguez-Fortea, A.; Alemany, P.; Ziegler, T. Density functional calculations of NMR chemical chifts with the inclusion of spin−orbit coupling in tungsten and lead compounds. *J. Phys. Chem. A* **1999**, *103*, 8288−8294.
(84) Krykunov, M.; Ziegler, T.; van Lenthe, E. Hybrid density functional calculations of nuclear magnetic shieldings using Slater-type orbitals and the zeroth-order regular approximation. *Int. J. Quantum Chem.* **2009**, *109*, 1676−1683.
(85) Wolff, S. K.; Ziegler, T.; van Lenthe, E.; Baerends, E. J. Density functional calculations of nuclear magnetic shieldings using the zeroth-order regular approximation (ZORA) for relativistic effects:

https://doi.org/10.1021/jacs.5c04759
J. Am. Chem. Soc. 2025, 147, 20865−20877

ZORA nuclear magnetic resonance. *J. Chem. Phys.* **1999**, *110*, 7689−7698.
(86) Autschbach, J.; Zurek, E. Relativistic density-functional computations of the chemical shift of ^{129}Xe in Xe@C_{60}. *J. Phys. Chem. A* **2003**, *107*, 4967−4972.
(87) Krykunov, M.; Ziegler, T.; van Lenthe, E. Implementation of a hybrid DFT method for calculating NMR shieldings using Slater-type orbitals with spin−orbital coupling included. applications to ^{187}Os, ^{195}Pt, and ^{13}C in heavy-metal complexes. *J. Phys. Chem. A* **2009**, *113*, 11495−11500.
(88) Adamo, C.; Barone, V. Toward reliable density functional methods without adjustable parameters: the PBE0 model. *J. Chem. Phys.* **1999**, *110*, 6158−6170.
(89) Lenthe, E. v.; Baerends, E. J.; Snijders, J. G. Relativistic regular two-component Hamiltonians. *J. Chem. Phys.* **1993**, *99*, 4597−4610.
(90) van Lenthe, E.; Baerends, E. J.; Snijders, J. G. Relativistic total energy using regular approximations. *J. Chem. Phys.* **1994**, *101*, 9783−9792.
(91) van Lenthe, E.; Baerends, E. J.; Snijders, J. G. Construction of the Foldy−Wouthuysen transformation and solution of the Dirac equation using large components only. *J. Chem. Phys.* **1996**, *105*, 2373−2377.
(92) van Lenthe, E.; van Leeuwen, R.; Baerends, E. J.; Snijders, J. G. Relativistic regular two-component Hamiltonians. *Int. J. Quantum Chem.* **1996**, *57*, 281−293.
(93) Visscher, L.; van Lenthe, E. On the distinction between scalar and spin−orbit relativistic effects. *Chem. Phys. Lett.* **1999**, *306*, 357−365.
(94) Autschbach, J. The role of the exchange-correlation response kernel and scaling corrections in relativistic density functional nuclear magnetic shielding calculations with the zeroth-order regular approximation. *Mol. Phys.* **2013**, *111*, 2544−2554.
(95) Adamo, C.; Barone, V. Toward chemical accuracy in the computation of NMR shieldings: the PBE0 model. *Chem. Phys. Lett.* **1998**, *298*, 113−119.
(96) van Lenthe, E.; Baerends, E. J. Optimized Slater-type basis sets for the elements 1−118. *J. Comput. Chem.* **2003**, *24*, 1142−1156.
(97) Becke, A. D. A multicenter numerical integration scheme for polyatomic molecules. *J. Chem. Phys.* **1988**, *88*, 2547−2553.
(98) Franchini, M.; Philipsen, P. H. T.; Visscher, L. The Becke fuzzy cells integration scheme in the Amsterdam Density Functional program suite. *J. Comput. Chem.* **2013**, *34*, 1819−1827.
(99) Glendening, E. D.; Landis, C. R.; Weinhold, F. Natural bond orbital methods. *WIREs Comput. Mol. Sci.* **2012**, *2*, 1−42.
(100) Glendening, E. D.; Landis, C. R.; Weinhold, F. NBO 7.0: New vistas in localized and delocalized chemical bonding theory. *J. Comput. Chem.* **2019**, *40*, 2234−2241.
(101) Medek, A.; Frydman, V.; Frydman, L. Central transition nuclear magnetic resonance in the presence of large quadrupole couplings: cobalt-59 nuclear magnetic resonance of cobaltophthalocyanines. *J. Phys. Chem. A* **1999**, *103*, 4830−4835.
(102) Bodart, P. R.; Amoureux, J.-P.; Dumazy, Y.; Lefort, R. Theoretical and experimental study of quadrupolar echoes for half-integer spins in static solid-state NMR. *Mol. Phys.* **2000**, *98*, 1545−1551.
(103) O'Dell, L. A.; Harris, K. J.; Schurko, R. W. Optimized excitation pulses for the acquisition of static NMR powder patterns from half-integer quadrupolar nuclei. *J. Magn. Reson.* **2010**, *203*, 156−166.
(104) Altenhof, A. R.; Lindquist, A. W.; Foster, L. D. D.; Holmes, S. T.; Schurko, R. W. On the use of frequency-swept pulses and pulses designed with optimal control theory for the acquisition of ultra-wideline NMR spectra. *J. Magn. Reson.* **2019**, *309*, No. 106612.
(105) Merwin, L. H.; Sebald, A. Cross-polarisation to low-γ nuclei: the first ^{183}W CPMAS spectra. *Solid State Nucl. Magn. Reson.* **1992**, *1*, 45−47.
(106) Cohen, A. J.; Mori-Sánchez, P.; Yang, W. Challenges for density functional theory. *Chem. Rev.* **2012**, *112*, 289−320.
(107) Wang, F.; Steimle, T. C.; Adam, A. G.; Cheng, L.; Stanton, J. F. The pure rotational spectrum of ruthenium monocarbide, RuC, and relativistic ab initio predictions. *J. Chem. Phys.* **2013**, *139*, 174318.
(108) Gusmão, E. F.; Santiago, R. T.; Haiduke, R. L. A. Accurate nuclear quadrupole moment of ruthenium from the molecular method. *J. Chem. Phys.* **2019**, *151*, 194306.
(109) Mishra, S. N. Ab-initio calculations of electric field gradient in Ru compounds and their implication on the nuclear quadrupole moments of ^{99}Ru and ^{101}Ru. *Pramana* **2017**, *89*, 22.
(110) Srebro, M.; Autschbach, J. Does a molecule-specific density functional give an accurate electron density? the challenging case of the CuCl electric field gradient. *J. Phys. Chem. Lett.* **2012**, *3*, 576−581.
(111) Srebro, M.; Autschbach, J. Computational analysis of $^{47/49}$Ti NMR shifts and electric field gradient tensors of half-titanocene complexes: structure−bonding−property relationships. *Chem. - Eur. J.* **2013**, *19*, 12018−12033.
(112) Grutzner, J. B.Chemical shift theory. Orbital symmetry and charge effects on chemical shifts. In *Recent advances in organic NMR spectroscopy*; Norell Press, 1987; pp 17−42.
(113) Autschbach, J.Analysis of NMR Spectroscopic Parameters. In *NMR spectroscopic parameters: Theories and models, computational codes and calculations*, Aucar, G. A., Ed.; Royal Society of Chemistry, in press.

https://doi.org/10.1021/jacs.5c04759
J. Am. Chem. Soc. 2025, 147, 20865−20877